Received: 27 May 2022 | Revised: 11 July 2022 | Accepted: 12 July 2022

DOI: 10.1002/agt2.258

Aggregate WILEY Open Access

RESEARCH ARTICLE

Modulation of dynamic aggregation in fluorogenic SNAP-tag probes for long-term super-resolution imaging

Qinglong Qiao[1] | **Wenjuan Liu**[1,2] | **Weijie Chi**[3] | **Jie Chen**[1,2] | **Wei Zhou**[1] | **Ning Xu**[1] | **Jin Li**[1] | **Xiangning Fang**[1,2] | **Yi Tao**[1,2] | **Yinchan Zhang**[1,2] | **Yingzhu Chen**[1] | **Lu Miao**[1] | **Xiaogang Liu**[3] | **Zhaochao Xu**[1]

[1]CAS Key Laboratory of Separation Science for Analytical Chemistry, Dalian Institute of Chemical Physics, Chinese Academy of Sciences, Dalian, China

[2]University of Chinese Academy of Sciences, Beijing, China

[3]Fluorescence Research Group, Singapore University of Technology and Design, Singapore, Singapore

Correspondence
Zhaochao Xu, CAS Key Laboratory of Separation Science for Analytical Chemistry, Dalian Institute of Chemical Physics, Chinese Academy of Sciences, 457 Zhongshan Road, Dalian 116023, China.
Email: zcxu@dicp.ac.cn

Funding information
National Natural Science Foundation of China, Grant/Award Numbers: 22078314, 21878286, 21908216; Dalian Institute of Chemical Physics, Grant/Award Numbers: DICPI202142, DICPI201938, DICPZZBS201805; Advanced Manufacturing and Engineering Program, Grant/Award Number: A2083c0051; Ministry of Education, Singapore, Grant/Award Number: MOE-MOET2EP10120-0007

Abstract

The combination of super-resolution microscopy and synthetic fluorescence probes has emerged as a universal tool to monitor dynamic biological events at the nanometer scale. However, the limited site-specificity and fluorogenicity of synthetic fluorescent probes make it still difficult to realize long-term super-resolution imaging. Herein, we introduce a dynamic aggregation mediated SNAP-tag fluorogenic probe, **BGAN-Aze**, which can specifically bind to various SNAP-tag fusion proteins with 41-fold fluorescence enhancement. The equilibrium between the non-fluorescent aggregate/dimer (A–D) and the fluorescent monomer (M) of **BGAN-Aze** acts as an effective method to reduce the fluorescence background and endow **BGAN-Aze** with the capability of conducting washing-free super-resolution imaging of various intracellular and extracellular proteins. Using this probe, we monitored multiple dynamic biological events, such as MMC, mitophagy, the fusion of nucleolus, and the growth and contact of filopodia. We expect that **BGAN-Aze** will become a widely used SNAP-tag for super-resolution imaging of dynamic biological events and the A–D–M equilibrium can be a general strategy for designing fluorogenic probes.

KEYWORDS
aggregation, dimer, fluorogenic, SNAP-tag, super-resolution imaging

1 | INTRODUCTION

Live cells are highly complex machines driven by a series of dynamic biological events. Our deep understanding of their inner mechanism critically depends on the visualization of dynamic cellular contents with high spatial and temporal resolution.[1] In recent years, the combination of fluorescence microscopy and synthetic fluorescence probes has successfully evolved as a universal tool to investigate these biological events in real-time or over a period of time.[2] Especially, the emerging super-resolution imaging has surpassed the optical diffraction limit and allowed the imaging of cellular contents at the nanometer scale.[3] However, a significant challenge in long-term super-resolution imaging of dynamic biological events still exists, as synthetic fluorescence probes always display limited site-specific labeling, cell permeability, and fluorogenicity in complex cellular environments.[4]

To improve the specificity of synthetic probes, self-labeling protein tags were proposed. These tags can be flexibly combined with various synthetic probes through specific enzymatic reactions, thus effectively exerting the optical properties of traditional organic fluorophores.[5] Nowadays, various protein fusion tags have been developed and widely used in labeling proteins of interest (POI), including HaloTag,[6] PYP-tag,[7] SNAP-tag,[8] TMP-tag,[9] and BL-tag.[10] One of the most prominent is SNAP-tag, an engineered variant of the human repair protein O^6-alkylguanine-DNA alkyltransferase (hAGT), which can specifically react with a broad variety of O^6-benzylguanine (BG) derivatives through the formation of a stable thioether bond.[8,11] Its diverse applications have been demonstrated in efficient and precise editing of endogenous transcripts,[12]

Qinglong Qiao and Wenjuan Liu contributed equally to this work.

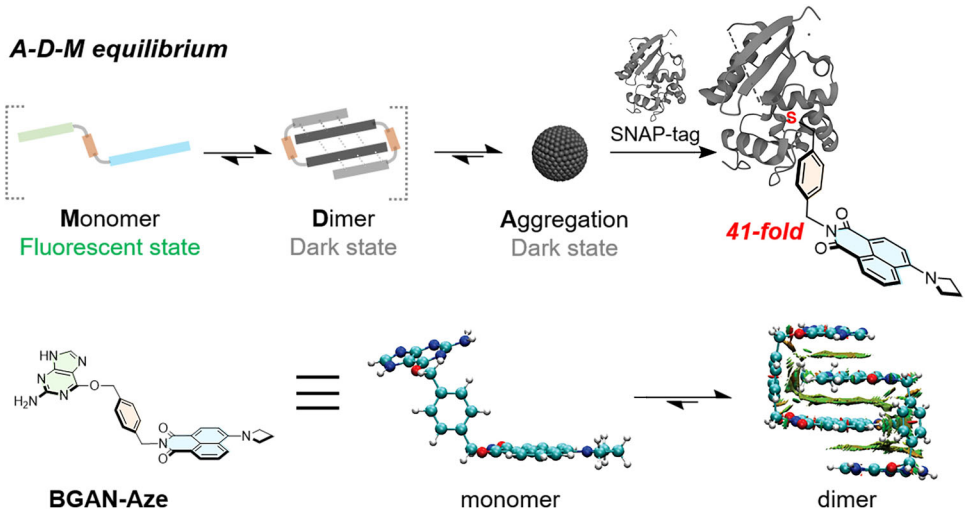

FIGURE 1 The proposed A–D–M equilibrium of fluorogenic SNAP-tag probe **BGAN-Aze**

super-resolution fluorescence imaging,[13] and biomolecular tracking inside living cells,[14] therefore generating extensive development of synthetic SNAP-tag probes.

However, most synthetic SNAP-tag probes exhibit high background and low cell permeability, which limit their applications in the study of dynamic biological events,[15] especially in long-term super-resolution imaging. These false signals from the background seriously affect the accurate judgment of the occurrence of biological events. Therefore, it is important to design fluorogenic SNAP-tag probes which show great increase in fluorescence upon the binding of SNAP-tags.[16] So far, several fluorescence activation strategies have been applied in constructing fluorogenic SNAP-tag probes, such as introducing quenchers,[17] inhibiting molecular twisting,[18] conjugating environment-sensitive fluorophores, and molecular switches.[19] Furthermore, controlling the assembly of synthetic probes evolves as an optimized way of tuning optical properties of dyes and enabling new design strategies for fluorescence tools including fluorogenic SNAP-tag probes.[20] Rhodamine dyes have nowadays become the preferred fluorophore for designing fluorogenic SNAP-tag probes for super-resolution imaging,[21] due to the equilibrium between a non-fluorescent spirocycle (L) form and a fluorescent zwitterion (Z) form.[22] The key factor for their fluorogenicity is that the aggregation of unreacted or unspecific binding of rhodamines to hydrophobic structures will stay in the non-fluorescent L-form, thereby reducing the background noise.[23] However, the L–Z equilibrium of rhodamine is severely affected by the charged microenvironment of POI and the linker length between rhodamine and BG group, since only negatively charged proteins cause the L-to-Z transition of rhodamines through electrostatic attraction.[24] Moreover, the BG and zwitterions rhodamine make it difficult to penetrate cell membranes and image intracellular contents at the nanometer scale. Therefore, there is an urgent need for fluorogenic SNAP-tag probes with universal labeling ability for different types of target proteins.

In this paper, we introduce a dynamic aggregation equilibrium, which triggers fluorescence "ON" and "OFF", to design a fluorogenic SNAP-tag probe **BGAN-Aze** used for wash-free long-term super-resolution imaging of dynamic biological events (Figure 1). The three components in **BGAN-Aze** of azetidine substituted naphthalimide, benzene ring, and guanine moieties are highly flat. Of particular importance, since the guannine group in the SNAP-tag substrate is prone to π–π interactions with chromophores,[25] this allows **BGAN-Aze** to adopt a U-shaped configuration to cross together to form a unique and fluorescence-quenched dimer. And due to the hydrophobic effect, dimers further aggregate to form spherical nanoparticles. The equilibrium between non-fluorescent aggregate/dimer (A–D) and fluorescent monomer (M), which always remain neutral, can enhance fluorogenicity and cell permeability simultaneously. Once **BGAN-Aze** reacts with SNAP-tag, its fluorescence will be activated and enhanced by 41-fold with the dissociation of the dimer. Compared with our previously reported naphthalimide-derived SNAP-tag probe **AN-BG** which can only fluorescently label mitochondria with high selectivity due to the formation of less stable aggregates only through hydrophobic interactions,[20] the formed stable and neutral dimer enables **BGAN-Aze** to rapidly penetrate membranes and has versatility for structural protein labeling and long-term super-resolution imaging of different intracellular organelles, including mitochondria, mitochondrial cristae, nucleolus, and filopodia. We further monitored the process of nucleolar fusion and its duration via super-resolution imaging for the first time. And the growth curve of filopodia was also successfully tracked in situ at the nanometer scale.

2 | RESULT AND DISCUSSION

2.1 | Existence of dimer and quenching effect

As the core regulatory trigger, A–D–M equilibrium was first demonstrated through high-resolution mass spectrometry (HRMS), computational analysis, fluorescence, and UV–vis absorption spectroscopy. First, we found an obvious dimer ion peak at 1011.3828 ($[2M+H]^+$, calculated 1011.3803, electrospray ionization as an ionization source) in the HRMS spectrum besides a monomer ion peak at 506.1958 ($[M+H]^+$, calculated 506.1941). These peaks prove the existence and high stability of the dimer (Figure 2A and Figure S1). In the meanwhile, a UV–vis absorption peak of the dimer at

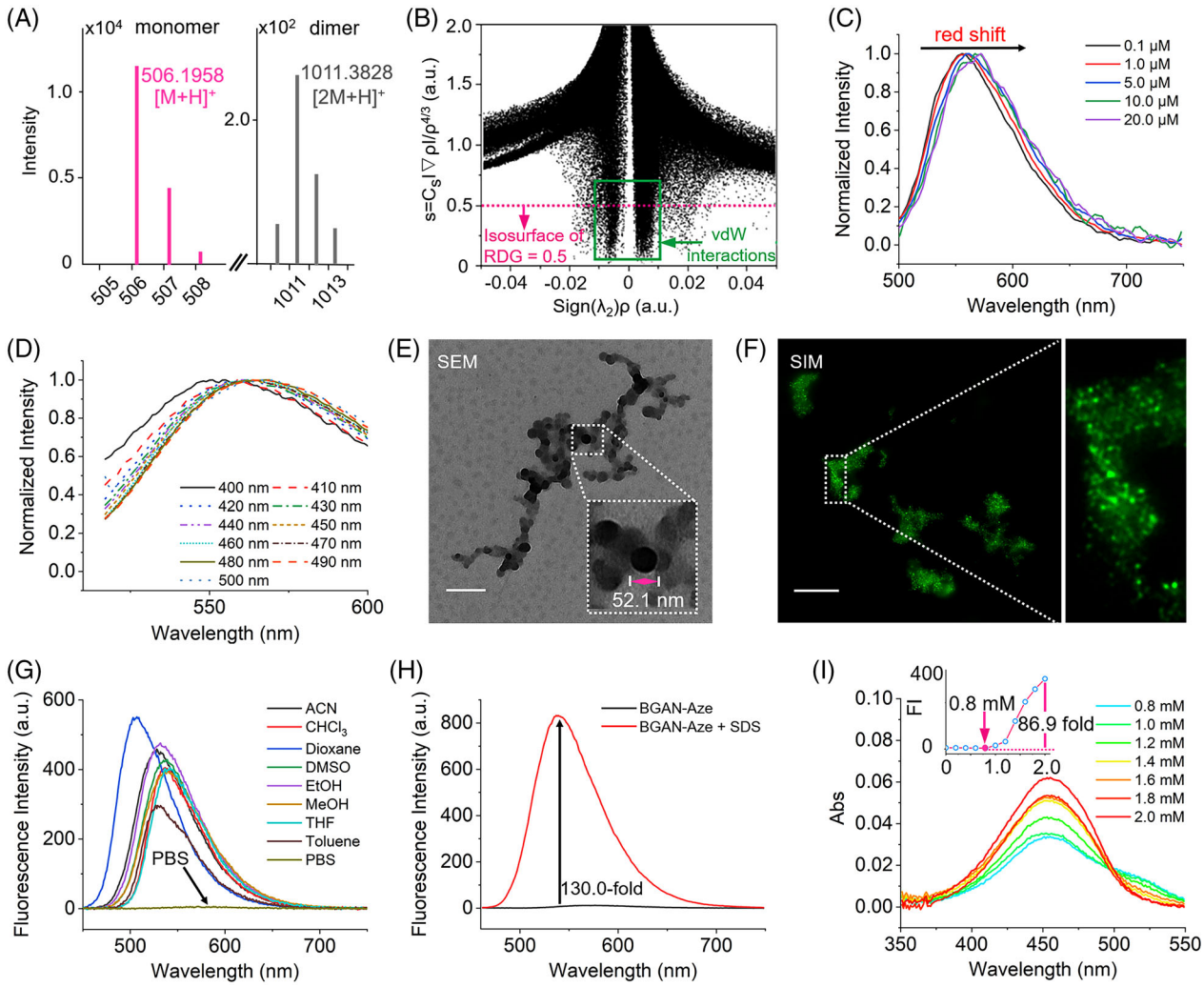

FIGURE 2 Characterization and quenching effect of dimer. (A) HRMS spectra of **BGAN-Aze** in high purity water. (B) Plots of the reduced density gradient *s* vs. the electron density multiplied by the sign of the second Hessian eigenvalue [sign(λ_2)ρ]. sign(λ_2)$\rho > 0$ denotes strong repulsion, sign(λ_2)$\rho < 0$ denotes strong attraction, and sign(λ_2)$\rho \approx 0$ denotes vdW interactions. (C) Fluorescence spectra of **BGAN-Aze** at various concentrations from 0.1 to 20 μM. (D) Fluorescence spectra of **BGAN-Aze** in phosphate-buffered saline (PBS) (20 mM, pH = 7.4), excited at various wavelengths from 400 to 500 nm (with a step size of 10 nm). (E) Scanning electron microscopy (SEM) imaging of aggregates of **BGAN-Aze**. Scale bar: 200 nm. (F) Structured illumination microscopy (SIM) imaging of aggregates of **BGAN-Aze** which were standing for 48 h in PBS (pH = 7.4, 20 mM). Scale bar: 5 μm. (G) Fluorescence spectra of **BGAN-Aze** in various solvents. [**BGAN-Aze**] = 10 μM. (H) Fluorescence spectra of 5 μM **BGAN-Aze** in the absence and the presence of 10 mM sodium dodecyl sulfate (SDS) in PBS (20 mM, pH = 7.4). (I) Absorption spectra of 5 μM **BGAN-Aze** with different concentration of SDS (0.8–2.0 mM) in PBS (20 mM, pH = 7.4). Inset: plot of the fluorescence intensity at 539 nm as a function of the concentration of SDS (0–2.0 mM)

525 nm was observed, in contrast to the monomer peak at 450 nm (Figure S2). The redshift in the dimer was consistent with our time-dependent density-functional theory calculations, which shows that the dimer of **BGAN-Aze** demonstrated a noticeable redshift in the UV–vis absorption spectrum, in comparison to that of the monomer (Figure S3). These results inspired us to simulate various aggregation conformations between two monomers of **BGAN-Aze** and explore its aggregation pattern, using molecular dynamics (MD) (Figure 2B and Figure S4–6). The most stable dimer conformation from the MD calculations was further optimized and analyzed with reference to a monomer, using density functional theory. Our results showed that both the azetidine-substituted naphthalimide (Figure S7, S31, crystal of a reference compound **AN-Aze**) and guanine moieties in **BGAN-Aze** were highly flat. Such a highly flat π-conjugated network afforded a strong tendency for aggregation. Consequently, two monomers of **BGAN-Aze** could form a "folded" dimer via van der Waal (vdW) and π–π interactions (Figure 1). The calculated intermolecular interaction energy (ΔE) amounts to −2.09 eV, indicating a substantial aggregation tendency. On the other side, we found that **BGAN-Aze** showed obvious redshifted absorption and emission compared with respect to the reference compound **AN-Aze** and **2** (**BGAN-Aze**: λ_{abs} = 470 nm, λ_{em} = 571 nm; **AN-Aze**: λ_{abs} = 465 nm, λ_{em} = 555 nm; **2**: λ_{abs} = 465 nm, λ_{em} = 557 nm) (Figures S8, S9, Table S1). Similarly, with the concentration of **BGAN-Aze** increasing in aqueous solution, the maximum absorption and emission wavelengths shifted from 556 nm (0.1 μM) to 572 nm (20.0 μM), which suggested that **BGAN-Aze** was apt to form J-aggregates (Figure 2C). This also could be confirmed by the normalized fluorescence spectra: as the excitation wavelength (λ_{ex}) shifted from 400 to 500 nm, the peak emission wavelength (λ_{em}) also progressively shifted from 545 to 570 nm (Figure 2D and Figure S10). A quite subtle excitation shoulder, which appeared at 490 nm, also became stronger when monitored at a longer emission wavelength (Figure S11). These

exceptional spectral profiles again demonstrated the J-aggregation of **BGAN-Aze**.

We also analyzed the nature of such strong intermolecular interactions, using the electron density and reduced density gradient (RDG) analysis developed by the Yang group,[26] whereby a small value of sign(λ_2)ρ close to 0 indicates vdW interactions. Indeed, our calculations revealed a low-density and low-gradient spike for the dispersion-bounded dimer, as highlighted in a green circle (Figure 2B). These results implied that vdW interactions are the main driving force for molecular aggregation. The vdW interactions could further promote the dimer of **BGAN-Aze** to form aggregate of nanoparticles, as confirmed by the dynamic light scattering (DLS) experiments (Figure S12). After standing for 48 h in phosphate-buffered saline (PBS), yellow aggregates formed and directly proved the larger aggregates of **BGAN-Aze** (Figure S13). SEM images also showed that **BGAN-Aze** aggregated to ~50 nm nanoparticles (Figure 2E) which could also be seen as weak fluorescent dots through super-resolution imaging (Figure 2F).

To validate the quenching effect of the dimer, we investigated the absorption and fluorescence spectra of **BGAN-Aze** and **AN-Aze** in different solvents (Figure 2G and Figure S8). Due to the sensitivity of naphthalimide to the microenvironment, their absorption wavelength and fluorescence wavelength all exhibited redshifts as the solvent polarity increased (Table S1). However, several differences between **BGAN-Aze** and **AN-Aze** are of note. The fluorescent brightness and molar extinction coefficient of **BGAN-Aze** decreased sharply in PBS, while **AN-Aze** kept moderate. Consequently, the quantum yield of **BGAN-Aze** was below 0.016 which was much lower than that of **AN-Aze** (0.20). It was indicated that the guanine group indeed made **BGAN-Aze** form dimer in PBS and the photo-induced electron transfer from guanine to naphthalimide quenched the fluorescence.

2.2 | Fluorogenicity of binding to SNAP-tag

The quenched aggregate/dimer of **BGAN-Aze** provided a novel strategy for designing fluorogenic probes toward SNAP-tags and encouraged us to investigate whether the aggregate/dimer could be disassembled and thereby recover high-fluorescence intensity simultaneously. With the addition of surfactant sodium dodecyl sulfate (SDS), the fluorescence of **BGAN-Aze** (5.0 μm in PBS, pH = 7.4) was greatly enhanced by more than 130 folds (Figure 2H and Figure S14, Table S2). On the contrary, the fluorescence intensity of **AN-Aze** only increased by less than three-folds at various concentrations of SDS from 0.1 to 20.0 μM (Figure S15). Surprisingly, we found the fluorescence enhancement mainly originated from the disassembly of dimer absorbing at 525 nm (Figure 2I and Figures S16 and S17). Upon the addition of SDS (0–0.8 mM), the aggregate of nanoparticles would first disassemble with a significant decrease at the absorption wavelength between 450–510 nm but negligible fluorescence enhancement (Figure S16). Subsequently, the dimer would gradually disassemble into monomer as more SDS was added (0.8–5 mM). Importantly, with the continuous decrease of absorption wavelength at 525 nm the fluorescence was enhanced greatly by 86.9 folds from 0.8 to 2.0 mM of SDS (Figure 2I). These results indicated that turn-on fluorescence response was driven by the disassembly of the aggregate/dimer and thus ensured its fluorogenicity to SNAP-tag.

We then used **BGAN-Aze** to label SNAP-tag in vitro and found the fluorescence intensity enhanced 41 folds after **BGAN-Aze** reacted with SNAP-tag which indicated excellent fluorogenicity for SNAP-tag (Figure 3A and Figure S18). DLS measurements further validated that **BGAN-Aze** (5.0 μM) aggregated into nanoparticles with a diameter around 600 nm in PBS (20 mM, pH = 7.4). These nanoparticles were indeed disassembled by SNAP-tag and the size decreased to ~4 nm after the conjugation to SNAP-tag (Figure 3B). The quantum yield of **BGAN-Aze** increased from 0.016 to 0.39 once binding to SNAP-tag (Table S1 and Figure 3A). It was worth noting that the emission wavelength of **BGAN-Aze** shifted to 540 nm from 571 nm after it bound to SNAP-tag (similar with the emission in MeOH at 540 nm). Since naphthalimide was a polarity-sensitive fluorophore (its emission experiences blueshifts with the decrease of polarity), we could speculate that the environment at the binding pocket of the SNAP-tag was highly polar. The protein labeling process was next monitored by recording the fluorescence intensity of **BGAN-Aze** at 535 nm to study the kinetics of the reaction rate, in which the total concentration of **BGAN-Aze** and SNAP-tag was 5 μM. And the time required for 50% labeling of SNAP-tag was about 56 s for **BGAN-Aze** (Figure 3C). The further kinetic analysis showed the second-order rate constant (K_2) of reaction between **BGAN-Aze** and SNAP-tag was 1998 ± 275 $M^{-1}s^{-1}$ (Figure S19). It indicated that the dimer of **BGAN-Aze** could be effectively disassembled by SNAP-tag along with great fluorescence enhancement.

2.3 | No-wash long-term super-resolution imaging in living cells using BGAN-Aze

Inspired by the above results, we demonstrated the low cytotoxicity (Figure S20) and high permeability (Figures S21 and S22) of **BGAN-Aze** beforehand, which ensured the success of wash-free fluorescence imaging of various intracellular proteins based on **BGAN-Aze**. First, live HeLa cells, expressing SNAP-vector, were incubated with **BGAN-Aze** for 30 min and directly imaged by confocal microscopy without washing step. Obvious green fluorescence was captured in the cytoplasm with good signal-to-noise ratio (13.0 folds) which indicated high cell permeability of **BGAN-Aze** that is available for intracellular proteins labeling (Figure 3D). On the contrary, non-transfected cells displayed negligible fluorescence. To further inspect the location accuracy of **BGAN-Aze** to SNAP-tag, commercialized plasmids pSNAPf-H2B, pSNAPf-Cox8A, pSNAPf-NPM1, and pSNAPf-ADRβ2 were transiently transfected to HeLa cells. It is satisfactory to observe strong fluorescence appearing in specific locations with a high signal-to-background ratio. Co-staining of **BGAN-Aze** and Hoechst 33342 was next performed which demonstrated that **BGAN-Aze** could light nuclear-localized SNAP-H2B with an excellent nuclei-to-cytosol signal ratio (~22.5 folds, Figure 3E, Figure S23). The intensity profiles of the linear regions across transfected cells displayed in close synchrony and further indicated colocalization between **BGAN-Aze** and Hoechst 33342.

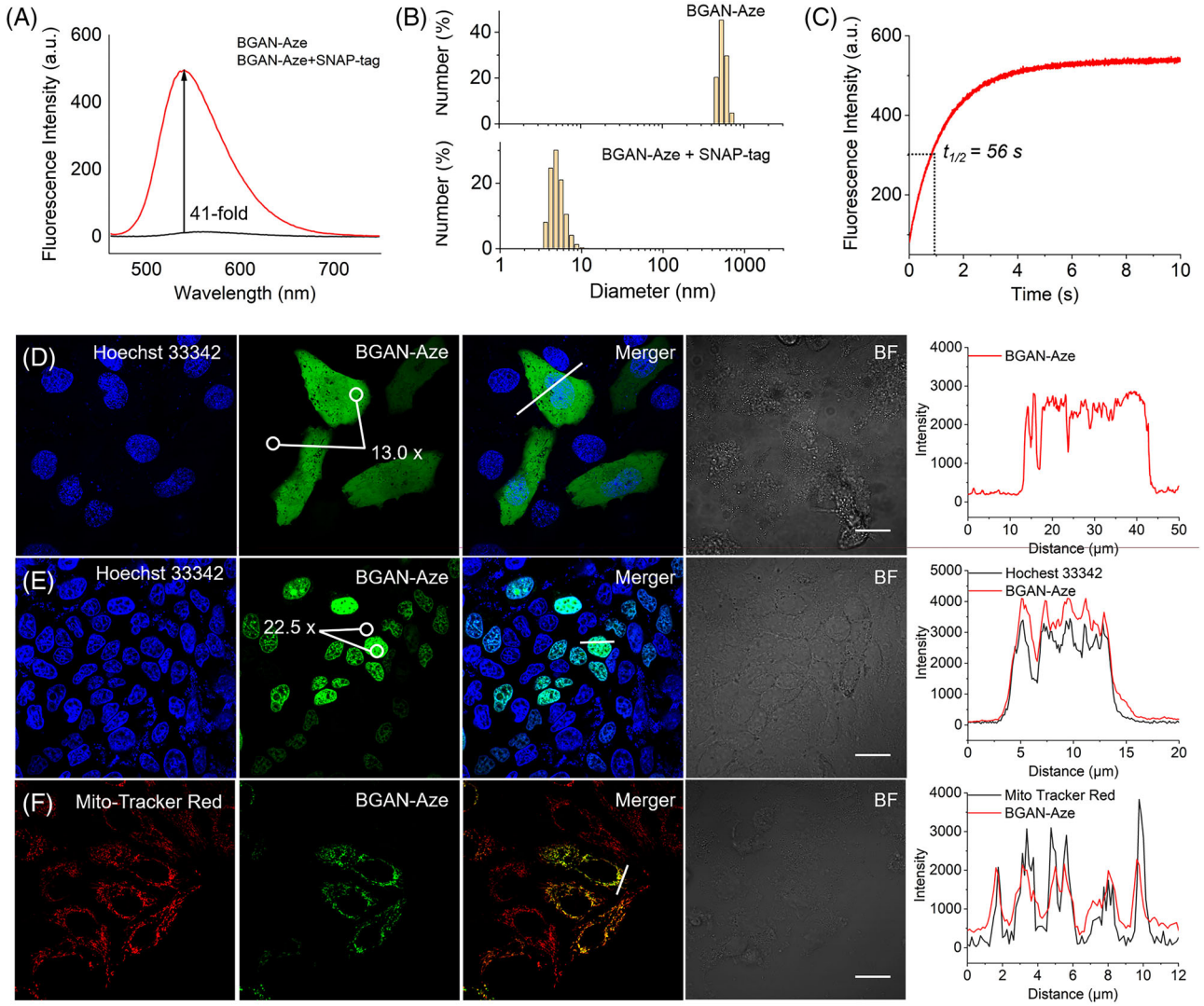

FIGURE 3 The response of **BGAN-Aze** to SNAP-tag. (A) Fluorescence spectra of 5 μM **BGAN-Aze** in the absence and the presence of 5 μM SNAP-tag. (B) DLS analysis of 5 μM **BGAN-Aze** in the absence and the presence of 5 μM SNAP-tag in PBS. (C) Time course of fluorescence intensity of 5 μM **BGAN-Aze** in the presence of equal purified SNAP-tag. (D–F) No-wash HeLa live-cell imaging of SNAP-tag proteins labeled with **BGAN-Aze**. HeLa cells transiently expressing SNAP-Vector, SNAP-H2B, and SNAP-Cox8A were incubated with 0.5 μM **BGAN-Aze** for 30 min. Graph: intensity profile of regions of interest (ROI) across cells. Scale bar: 20 μm

Moreover, the labeling of SNAP-Cox8A, SNAP-ADRβ2, and pSNAPf-NPM1 fusion proteins with **BGAN-Aze** revealed mitochondrial, membranal, and nucleolar outlines for its excellent fluorogenicity and location accuracy (Figure 3F and Figures S24 and S25). These results suggest that **BGAN-Aze** is highly suited for the visualization of various proteins at a specific location without a washing procedure.

The excellent performance of our probe in imaging different types of target proteins prompted us to investigate its application in long-term super-resolution imaging of different organelles and subcellular organelles (Figure S26). Mitochondria are highly dynamic organelles. They are highly sensitive to phototoxicity, as reflected by a significant change in membrane potential (Figure S27). This makes many mitochondrial probes incompatible in long-term super-resolution imaging. Because these probes are lipophilic cations and target mitochondria depend on the negative mitochondrial membrane potential. Once the mitochondrial membrane potential is lost, a mass of probes will dissociate into the cytoplasm and induce high background fluorescence. Therefore, we intended to inspect the performance of our probe, which could target mitochondria inner membrane through forming a stable thioether bond with SNAP-Cox8A fusion proteins, in long-term structured illumination microscopy (SIM) imaging and explore mitochondrial dynamics.

Mitochondrial cristae, formed by the inner membrane of mitochondria, are highly dynamic sub-organelle structures that are still challenging for super-resolution imaging. As they house the megadalton complexes of the electron transport chain and adenosine triphosphate synthase, their morphologies are recognized as an evaluation criterion for mitochondrial health. As shown in Figure 4, due to its specific location in the inner membrane, **BGAN-Aze** could clearly image mitochondrial cristae via SIM (Figures 4, A1–6). Most of the cristae were perpendicular to the mitochondrial macro axis and formed sheet-like mitochondrial cristae. However, there existed a large empty space, labeled by white arrows in A1–6, at the junctions of mitochondria. To monitor the dynamic network of mitochondrial cristae, we tracked single branching mitochondrion under super-resolution imaging for 10 min. Figure 4B showed the tanglesome mitochondrial

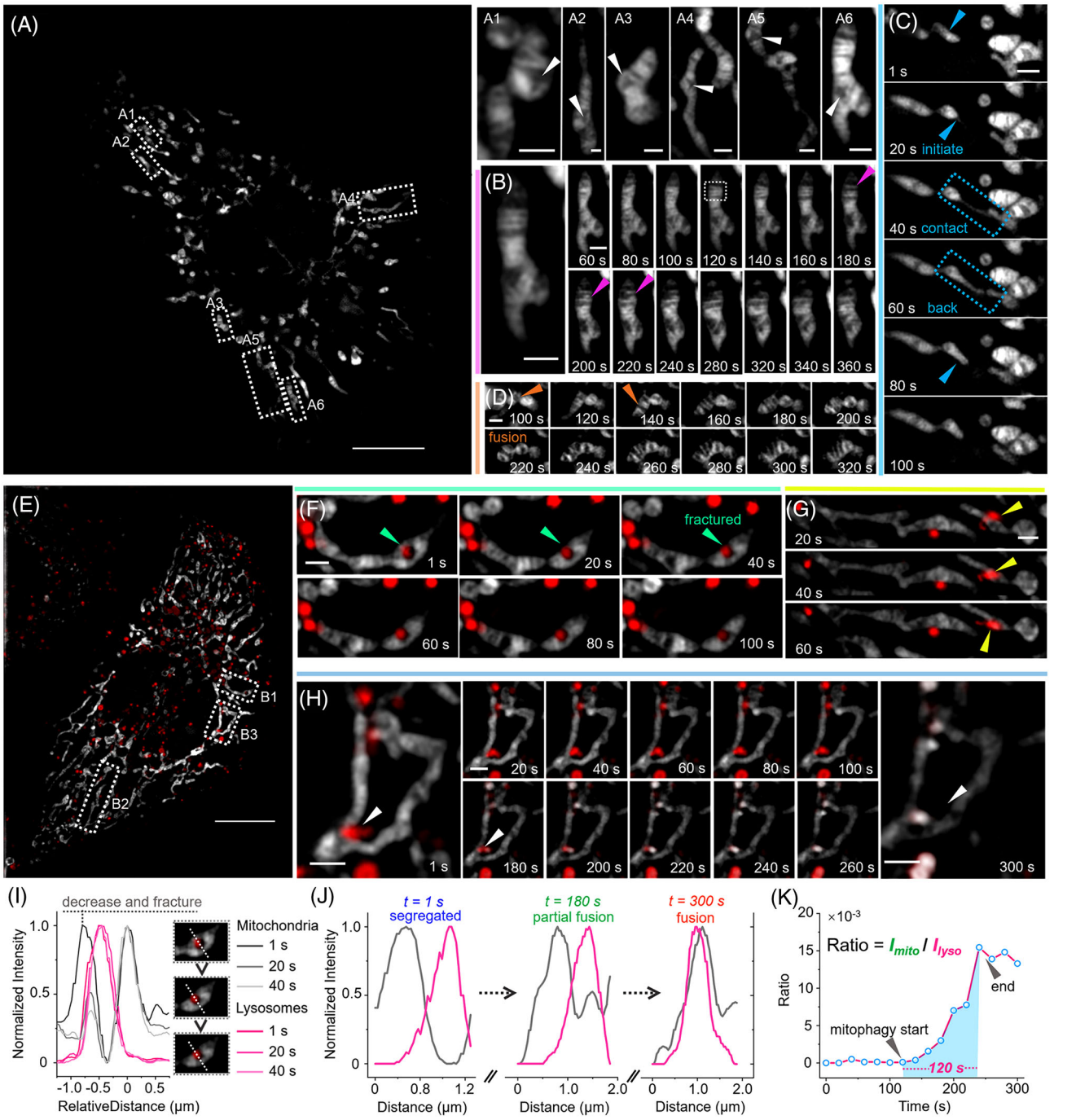

FIGURE 4 Super-resolution imaging of mitochondria in living HeLa cells which were incubated with 0.5 μM **BGAN-Aze** for 30 min. **BGAN-Aze** λ_{ex} = 488 nm, collected: 500–545 nm; Lyso-Tracker Red λ_{ex} = 561 nm, collected: 570–640 nm. (A–H) SIM imaging of mitochondria and mitochondrial cristae based on SNAP-tag-Cox8A fusion protein labeled with **BGAN-Aze**. (A,E) Scale bar: 10 μm. A1–6, (B–D), (F–H) Scale bar: 1.0 μm. (I) Intensity profile of regions of interest (ROI) across mitochondria and lysosome in (F). (J) Intensity profile of ROI across mitochondria and lysosome in (H) at different time points. (K) Time dependence of the ratios of fluorescence intensities I_{mito} and I_{lyso}

cristae at 40 s gradually changed into lamellar ones during 40–120 s. It was worth noting that the three sheet-like mitochondrial cristae in dashed box arranged parallelly and kept close or far away from time to time. While, some of them, labeled by pink arrows in Figure 4B, fractured into smaller sheets at 200 s. As a consequence, the network of mitochondrial cristae was highly dynamic and could be imaged by our probe at the nanometer scale. Furthermore, the instantaneous contact between two isolated mitochondria was also observed in Figure 4C. Mitochondria, labeled by a blue arrow in Figure 4C, turned into a round one and stretched vimineous "tentacle" like branch toward right mitochondria at 20 s, simultaneously. In the blue dashed frame, intimate contact was captured during 40–60 s. The two mitochondria soon separated at 60 s and returned to the initial state. These results inspired us to further chase the change of mitochondrial cristae during the mitochondria–mitochondria interaction. Fortunately, we monitored the fusion of two mitochondria during 100–240 s (Figure 4D). At 100 s, the two mitochondria approached each other showing the intimate contact. As the event went on, the left mitochondrion displayed a clear sheet and gradually turned into a rotund one from a clubbed one, along with the disappearance of many mitochondrial cristae. However, after complete fusion at 240 s, the newly formed

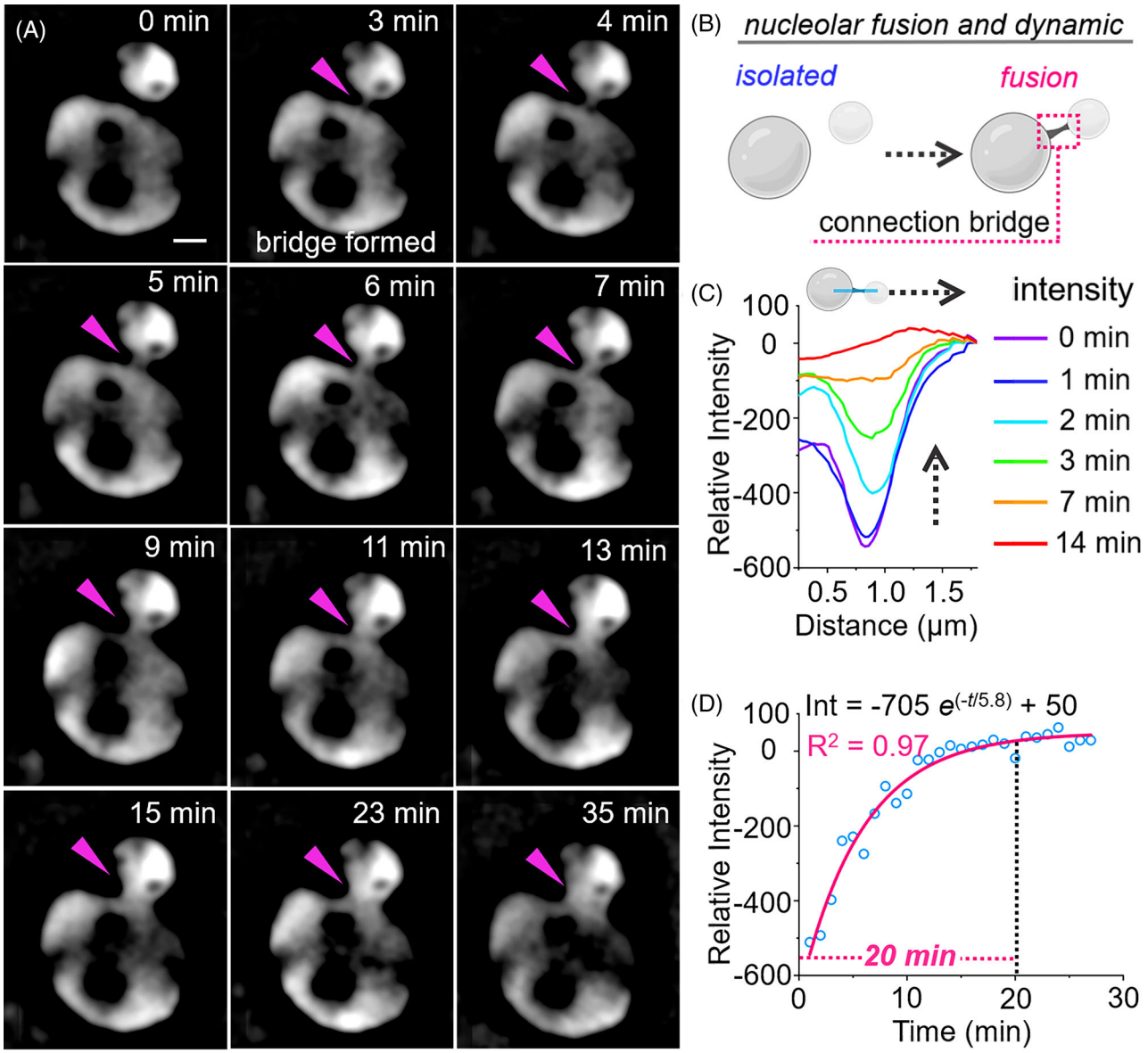

FIGURE 5 Super-resolution imaging of nucleolar fusion in living HeLa cells which were incubated with 0.5 μM **BGAN-Aze** for 30 min. λ_{ex} = 488 nm, collected: 500–545 nm. (A) SIM imaging of nucleolus based on SNAP-tag-NPM1 fusion protein labeled with **BGAN-Aze**. Scale bar: 1.0 μm. (B) Schematic diagram for the nucleolar fusion and connection bridge formation. (C) Relative intensity profile of connection bridge at different time points. (D) Time dependence of the maximum fluorescence intensities in (C)

mitochondrion again showed distinct lamellar mitochondrial cristae.

Although mitochondria are considered as semi-autonomous organelles, they also engaged in many physiological processes via dynamic interactions with other subcellular organelles, including fission, mitophagy, and apoptosis. As mitophagy acts as a crucial role in cellular stress caused by aberrant oxidative bursts in which damaged mitochondria are removed by autolysosomes, we next carried out long-term dual-color SIM imaging to reveal the dynamic interactions between mitochondria and lysosomes (Figure 4E). The mitochondria were stained with our probe and lysosomes were labeled with Lyso-Tracker Red, respectively. As shown in Figure 4F, the lysosome, lined out by a green arrow, was stranded in the center of the annular mitochondrion and displayed intimate contact with each other. While at 20 s the annular mitochondrion was gradually cut off at the contact site and turned into a linear one. The intensity profiles of the linear regions in Figure 4I further indicated the left section of the annular mitochondrion gradually disappeared with the decrease of fluorescence intensity. Moreover, some prolonged contacts between lysosomes and mitochondria had been captured. The lysosome in Figure 4G moved around a linear mitochondrion (marked by a yellow arrow) and showed frequent contact during 1–100 s (Figure S28). While another lysosome remained motionless at an unchanged contact site. Due to the stable covalent labeling of **BGAN-Aze** to mitochondria, mitophagy was monitored in which damaged mitochondria would be phagocytosed by acidic lysosomes. It was shown in Figure 4H that the lysosome kept close contact with the joint of mitochondrion during 1–300 s. But we could observe the red lysosome, marked by white arrow, gradually changed to light grey. The intensity profiles across the lysosome and mitochondrion in Figure 4J, which showed separated signals at 1 s, increasingly exhibited co-localization and indicated partial mitochondrion fused with this lysosome and the occurrence of mitophagy. We also calculated the ratio of

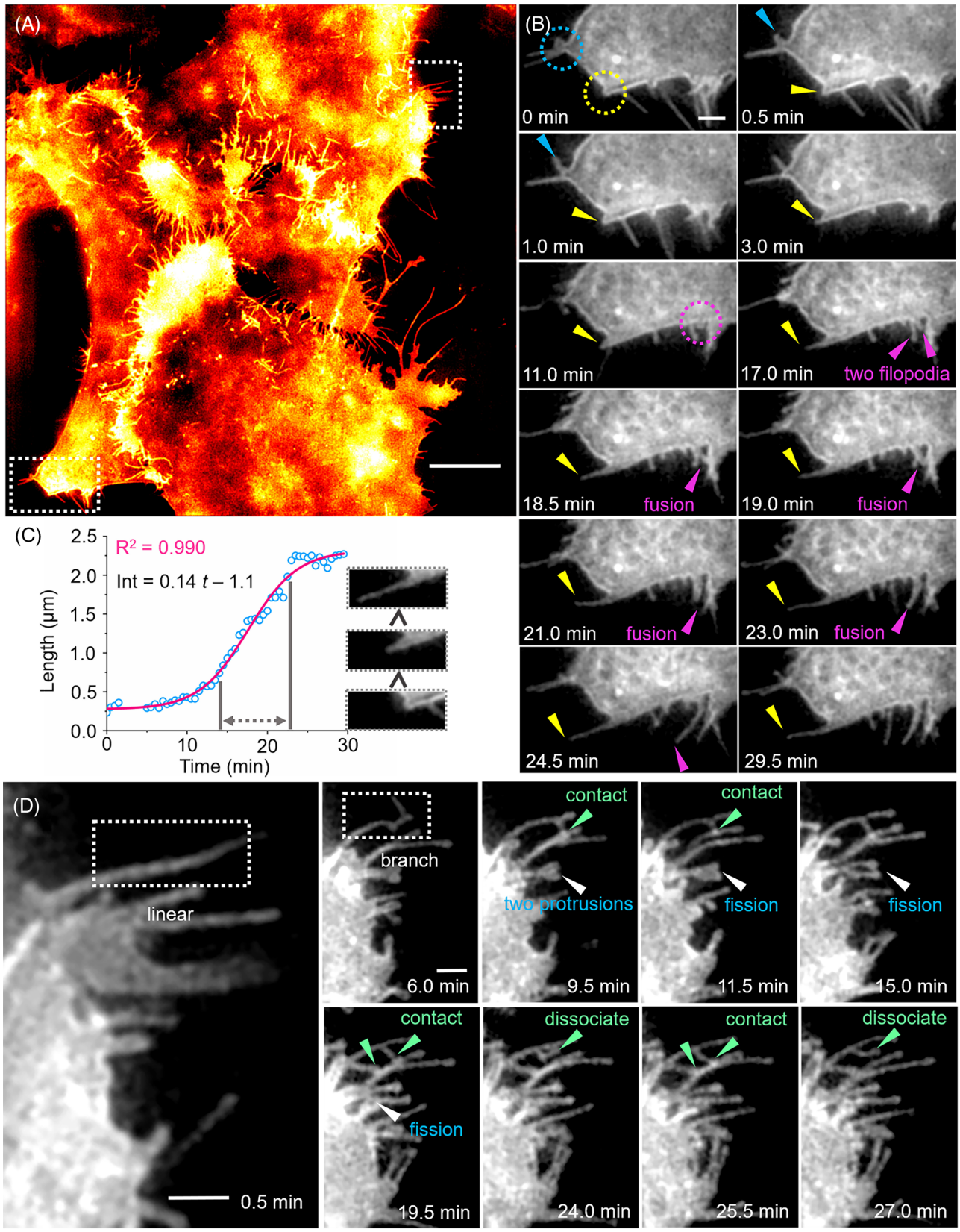

FIGURE 6 Super-resolution imaging of plasma-membrane in living HeLa cells which were incubated with 0.2 μM **BGAN-Aze** for 10 min. λ_{ex} = 488 nm, collected: 500–545 nm. (A,B,D) SIM imaging of cytomembrane based on SNAP-tag-ADRβ2 fusion protein labeled with **BGAN-Aze**. (C) Time dependence of the length of filopodia labeled by a yellow arrow in (B). (A) Scale bar: 10 μm. (BC) Scale bar: 1.0 μm

I_{mito} to I_{lyso} (Figure 4K) and inspected the whole process of mitophagy which indicated the process lasted about 120 s. These results demonstrated the ability of **BGAN-Aze** in long-term super-resolution imaging of mitochondrial dynamics for its excellent specificity, stability, and fluorogenicity.

As the largest membrane-less organelle, nucleolar fission and fusion act crucial roles in the liquid–liquid phase separation (LLPS). However, it is still difficult to imagine the whole process of fusion at the nanometer scale because of its long duration.[27] Inspired by the successful application in

long-term super-resolution imaging, we monitored the overall process of nucleolar fusion at the nanometer scale for the first time and found that the process lasted ~20 min (Figure 5 and Figure S25). As shown in Figure 5A, the two nucleoli appeared completely separated at 0 min and formed a connection bridge at 3 min which gradually became bulky (Figure 5B). Furthermore, relative fluorescence intensity was adopted to further illustrate the formation of the connection bridge (Figure S29). The intensity between the initial two nucleoli continuously increased until almost equal to the intensity of the two nucleoli which indicated the formation of a stable connection bridge (Figure 5C). The increase of fluorescence intensity at the distance of 800 nm was analyzed in Figure 5D and indicated that the process lasted about 20 min. We also observed the behavior of H2B, a major protein in chromatin, at the nanometer scale for 8 h (Figures S26 and S30).

Besides intracellular proteins, we also tracked membranal dynamics through SNAP-ADRβ2 in which SNAP-tag was exposed to the extracellular side of the membrane (Figure 6). As plasma-membrane protrusions, filopodia primarily work as antennae to probe the surrounding environment which is involved in many biological events such as cell migration, wound healing, and neurite outgrowth.[28] However, filopodia are highly dynamic with a nanometer size, and their growth rate is still unclear. Fortunately, using **BGAN-Aze** we observed the whole growth process of several filopodia and calculated their growth rate (Figure 6A,B). At 0 min, two subtle bulges, marked by blue and yellow circles, appeared as growth sites for filopodia. The bulge, labeled by a blue arrow in Figure 6B, first stretched out the filiform bubble and extended 0.95 μm after 1 min. Differently, the bulge, which was labeled by a yellow arrow, underwent a long-term growth process during 5–24 min. Through the time-dependent growth curve, we could find that the growth rate was dynamically changing and appeared slow in the initial stage (Figure 6C). Moreover, another growth model was captured. Bulge marked by a pink arrow was formed at 11 min and fused with lateral mature filopodia during 17–23 min. Then, the newly syncretic filopodia continued to extend 0.62 μm during 23–24.5 min. Besides the formation of fresh filopodia through original protrusions and fusion, filopodia could also be newly formed by the fission of mature filopodia (Figure 6D). The intact filopodia, labeled by white arrows, showed obvious protrusions at 9.5 min which split into two filopodia during 9.5–19.5 min and indicated the fission of mature filopodia. In addition, morphological changes of filopodia were captured that the filopodia which displayed linear at 0.5 min in the dashed box turned into dendritic one showing fickle morphology. The aforementioned filopodia also showed close contact with the adjacent filopodia at the sites labeled by green arrows during 9.5–23.5 min and dissociated at 24 min. Unlike the prolonged contact shown above, it re-contacted the same filopodia at 25.5 min and dissociated at 27 min showing less than 1.5 min contact time.

3 | CONCLUSION

In conclusion, through the A–D-M equilibrium of **BGAN-Aze,** we developed a fluorogenic SNAP-tag probe and realized long-term super-resolution imaging of universal intracellular and extracellular proteins. **BGAN-Aze** forms quenched aggregates with minimal background fluorescence. Upon binding to the SNAP-tag, the fluorescence of **BGAN-Aze** increased by 41-fold, as a result of the dissociation of the aggregate. Finally, **BGAN-Aze** was successfully applied to long-term super-resolution imaging of dynamic mitochondrial cristae, nucleolus, and filopodia, and revealed various dynamic biological events, including mitochondria–mitochondria contact (MMC), mitophagy, the fusion of nucleolus, growth, and contact of filopodia. We believe that the A–D–M equilibrium as shown in **BGAN-Aze** will become a promising new strategy for developing fluorogenic probes.

ACKNOWLEDGMENTS

This work is supported by the National Natural Science Foundation of China (22078314, 21878286, 21908216) and Dalian Institute of Chemical Physics (DICPI202142, DICPI201938, DICPZZBS201805). The authors thank the support from A*STAR under its Advanced Manufacturing and Engineering Program (A2083c0051), the Ministry of Education, Singapore (MOE-MOET2EP10120-0007).

CONFLICT OF INTEREST

The authors declare that there is no conflict of interest that could be perceived as prejudicing the impartiality of the research reported.

ORCID

Weijie Chi https://orcid.org/0000-0003-1776-0025
Zhaochao Xu https://orcid.org/0000-0002-2491-8938

REFERENCES

1. C. Li, A. G. Tebo, A. Gautier, *Int. J. Mol. Sci.* **2017**, *18*, 1473.
2. a) L. Wang, W. Du, Z. Hu, K. Uvdal, L. Li, W. Huang, *Angew. Chem. Int. Ed.* **2019**, *58*, 14026; b) J. B. Grimm, A. K. Muthusamy, Y. Liang, T. A. Brown, W. C. Lemon, R. Patel, R. Lu, J. J. Macklin, P. J. Keller, N. Ji, L. D. Lavis, *Nat. Methods* **2017**, *14*, 987.
3. a) G. Lukinavičius, K. Umezawa, N. Olivier, A. Honigmann, G. Yang, T. Plass, V. Mueller, L. Reymond, I. R. Corrêa Jr, Z.-G. Luo, C. Schultz, E. A. Lemke, P. Heppenstall, C. Eggeling, S. Manley, K. Johnsson, *Nat. Chem.* **2013**, *5*, 132; b) S. A. Jones, S.-H. Shim, J. He, X. Zhuang, *Nat. Methods* **2011**, *8*, 499; c) G. Vicidomini, P. Bianchini, A. Diaspro, *Nat. Methods* **2018**, *15*, 173.
4. a) Q. Qiao, W. Liu, J. Chen, X. Wu, F. Deng, X. Fang, N. Xu, W. Zhou, S. Wu, W. Yin, X. Liu, Z. Xu, *Angew. Chem. Int. Ed.* **2022**, *61*, e202202961. https://doi.org/10.1002/anie.202202961; b) J. Chen, C. Wang, W. Liu, Q. Qiao, H. Qi, W. Zhou, N. Xu, J. Li, H. Piao, D. Tan, X. Liu, Z. Xu, *Angew. Chem. Int. Ed.* **2021**, *60*, 25104; c) X. Li, J. Zheng, W. Liu, Q. Qiao, J. Chen, W. Zhou, Z. Xu, *Chin. Chem. Lett.* **2020**, *31*, 2937.
5. a) C. Jing, V. W. Cornish, *Acc. Chem. Res.* **2011**, *44*, 784; b) K. M. Marks, G. P. Nolan, *Nat. Methods* **2006**, *3*, 591; c) J. B. Grimm, L. D. Lavis, *Nat. Methods* **2022**, *19*, 149.
6. G. V. Los, L. P. Encell, M. G. McDougall, D. D. Hartzell, N. Karassina, C. Zimprich, M. G. Wood, R. Learish, R. F. Ohana, M. Urh, D. Simpson, J. Mendez, K. Zimmerman, P. Otto, G. Vidugiris, J. Zhu, A. Darzins, D. H. Klaubert, R. F. Bulleit, K. V. Wood, *ACS Chem. Biol.* **2008**, *3*, 373.
7. a) Y. Hori, H. Ueno, S. Mizukami, K. Kikuchi, *J. Am. Chem. Soc.* **2009**, *131*, 16610; b) Y. Hori, K. Nakaki, M. Sato, S. Mizukami, K. Kikuchi, *Angew. Chem. Int. Ed.* **2012**, *51*, 5611.
8. A. Keppler, S. Gendreizig, T. Gronemeyer, H. Pick, H. Vogel, K. Johnsson, *Nat. Biotechnol.* **2003**, *21*, 86.
9. a) Z. Chen, C. Jing, S. S. Gallagher, M. P. Sheetz, V. W. Cornish, *J. Am. Chem. Soc.* **2012**, *134*, 13692; b) L. W. Miller, Y. Cai, M. P. Sheetz, V. W. Cornish, *Nat. Methods* **2005**, *2*, 255; c) C. Jing, V. W. Cornish, *ACS Chem. Biol.* **2013**, *8*, 1704.

10. S. Mizukami, S. Watanabe, Y. Hori, K. Kikuchi, *J. Am. Chem. Soc.* **2009**, *131*, 5016.
11. A. Keppler, H. Pick, C. Arrivoli, H. Vogel, K. Johnsson, *Proc. Natl. Acad. Sci. USA* **2004**, *101*, 9955.
12. P. Vogel, M. Moschref, Q. Li, T. Merkle, K. D. Selvasaravanan, J. B. Li, T. Stafforst, *Nat. Methods* **2018**, *15*, 535.
13. S.-n. Uno, M. Kamiya, T. Yoshihara, K. Sugawara, K. Okabe, M. C. Tarhan, H. Fujita, T. Funatsu, Y. Okada, S. Tobita, Y. Urano, *Nat. Chem.* **2014**, *6*, 681.
14. P. J. Bosch, I. R. Corrêa, M. H. Sonntag, J. Ibach, L. Brunsveld, J. S. Kanger, V. Subramaniam, *Biophys. J.* **2014**, *107*, 803.
15. T. Komatsu, K. Johnsson, H. Okuno, H. Bito, T. Inoue, T. Nagano, Y. Urano, *J. Am. Chem. Soc.* **2011**, *133*, 6745.
16. S. I. Reja, M. Minoshima, Y. Hori, K. Kikuchi, *J. Biol. Inorg. Chem.* **2019**, *24*, 443.
17. a) X. Sun, A. Zhang, B. Baker, L. Sun, A. Howard, J. Buswell, D. Maurel, A. Masharina, K. Johnsson, C. J. Noren, M.-Q. Xu, I. R. Corrêa Jr., *Chembiochem* **2011**, *12*, 2217; b) C.-J. Zhang, L. Li, G. Y. J. Chen, Q.-H. Xu, S. Q. Yao, *Org. Lett.* **2011**, *13*, 4160.
18. a) K. H. Jung, M. Fares, L. S. Grainger, C. H. Wolstenholme, A. Hou, Y. Liu, X. Zhang, *Org. Biomol. Chem.* **2019**, *17*, 1906; b) W.-T. Yu, T.-W. Wu, C.-L. Huang, I. C. Chen, K.-T. Tan, *Chem. Sci.* **2016**, *7*, 301.
19. a) T.-K. Liu, P.-Y. Hsieh, Y.-D. Zhuang, C.-Y. Hsia, C.-L. Huang, H.-P. Lai, H.-S. Lin, I. C. Chen, H.-Y. Hsu, K.-T. Tan, *ACS Chem. Biol.* **2014**, *9*, 2359; b) K. Stöhr, D. Siegberg, T. Ehrhard, K. Lymperopoulos, S. Öz, S. Schulmeister, A. C. Pfeifer, J. Bachmann, U. Klingmüller, V. Sourjik, D.-P. Herten, *Anal. Chem.* **2010**, *82*, 8186; c) E. Prifti, L. Reymond, M. Umebayashi, R. Hovius, H. Riezman, K. Johnsson, *ACS Chem. Biol.* **2014**, *9*, 606.
20. a) T.-C. Hou, Y.-Y. Wu, P.-Y. Chiang, K.-T. Tan, *Chem. Sci.* **2015**, *6*, 4643; b) W. Liu, Q. Qiao, J. Zheng, J. Chen, W. Zhou, N. Xu, J. Li, L. Miao, Z. Xu, *Biosens. Bioelectron.* **2021**, *176*, 112886.
21. a) N. Lardon, L. Wang, A. Tschanz, P. Hoess, M. Tran, E. D'Este, J. Ries, K. Johnsson, *J. Am. Chem. Soc.* **2021**, *143*, 14592; b) Z. Ye, H. Yu, W. Yang, Y. Zheng, N. Li, H. Bian, Z. Wang, Q. Liu, Y. Song, M. Zhang, Y. Xiao, *J. Am. Chem. Soc.* **2019**, *141*, 6527.
22. a) J. B. Grimm, A. N. Tkachuk, L. Xie, H. Choi, B. Mohar, N. Falco, K. Schaefer, R. Patel, Q. Zheng, Z. Liu, J. Lippincott-Schwartz, T. A. Brown, L. D. Lavis, *Nat. Methods* **2020**, *17*, 815; b) J. B. Grimm, T. A. Brown, A. N. Tkachuk, L. D. Lavis, *ACS Cent. Sci.* **2017**, *3*, 975; c) W. Zhou, X. Fang, Q. Qiao, W. Jiang, Y. Zhang, Z. Xu, *Chin. Chem. Lett.* **2021**, *32*, 943.
23. G. Lukinavicius, K. Umezawa, N. Olivier, A. Honigmann, G. Yang, T. Plass, V. Mueller, L. Reymond, I. R. Correa Jr., Z. G. Luo, C. Schultz, E. A. Lemke, P. Heppenstall, C. Eggeling, S. Manley, K. Johnsson, *Nat. Chem.* **2013**, *5*, 132.
24. L. Wang, M. Tran, E. D'Este, J. Roberti, B. Koch, L. Xue, K. Johnsson, *Nat. Chem.* **2020**, *12*, 165.
25. Z. Xu, N. J. Singh, J. Lim, J. Pan, H. N. Kim, S. Park, K. S. Kim, J. Yoon, *J. Am. Chem. Soc.* **2009**, *131*, 15528.
26. E. R. Johnson, S. Keinan, P. Mori-Sánchez, J. Contreras-García, A. J. Cohen, W. Yang, *J. Am. Chem. Soc.* **2010**, *132*, 6498.
27. a) C. M. Caragine, S. C. Haley, A. Zidovska, *eLife* **2019**, *8*, e47533; b) C. M. Caragine, S. C. Haley, A. Zidovska, *Phys. Rev. Lett.* **2018**, *121*, 148101.
28. P. K. Mattila, P. Lappalainen, *Nat. Rev. Mol. Cell Biol.* **2008**, *9*, 446.

SUPPORTING INFORMATION

Additional supporting information can be found online in the Supporting Information section at the end of this article.

How to cite this article: Q. Qiao, W. Liu, W. Chi, J. Chen, W. Zhou, N. Xu, J. Li, X. Fang, Y. Tao, Y. Zhang, Y. Chen, L. Miao, X. Liu, Z. Xu, *Aggregate* **2023**, *4,* e258. https://doi.org/10.1002/agt2.258